



Cite this: DOI: 10.1039/d3me00086a

# Accurate calculation of second osmotic virial coefficients of proteins using mixed Poisson–Boltzmann and extended DLVO theory†

 Srdjan Pusara,  Wolfgang Wenzel  and Mariana Kozłowska \*

The state of proteins in aqueous solution is determined by weak, nonspecific interactions affected by pH, solvent composition, and ionic strength. Protein–protein interactions play a crucial role in determining protein stability and solubility. The second osmotic coefficient ( $B_{22}$ ) provides insight into effective interactions between proteins in solution. Models for calculating  $B_{22}$  are valuable for estimating interactions, explaining measured phenomena, and reducing experimental time. However, existing models, like the Derjaguin–Landau–Verwey–Overbeek (DLVO) theory, assume a simple spherical shape for proteins. Owing to the fact that proteins exhibit diverse shapes and charge distributions, influencing their electrostatic properties and overall interactions, DLVO accuracy is significantly reduced for nonspherical proteins. To address this limitation, we introduce the xDLVO-CGhybr model, which combines Poisson–Boltzmann (PB) and Debye–Hückel (DH) theories to account for electrostatic interactions between proteins. PB is used for short intermolecular distances (<2 nm) with an all-atom resolution, while DH is employed for longer distances on a coarse-grained level. Additionally, xDLVO-CGhybr incorporates an improved coarse-grained Lennard–Jones (LJ) potential derived directly from the all-atom potential to capture dispersion interactions. This model improves the calculated  $B_{22}$  values compared to existing models and can be applied to proteins with arbitrary shape and charge under various solvent conditions (up to 1 M monovalent salt concentration). We demonstrate the application of xDLVO-CGhybr to bovine trypsin inhibitor, ribonuclease A, chymotrypsinogen, concanavalin A, bovine serum albumin, and human immunoglobulin type I proteins, validating the model against experimental data.

 Received 31st May 2023,  
 Accepted 3rd July 2023

DOI: 10.1039/d3me00086a

[rsc.li/molecular-engineering](https://rsc.li/molecular-engineering)

## Design, System, Application

Proteins, as complex macromolecules, exhibit diverse structures, functions, and sizes, making them the most versatile biological species. Understanding protein behaviour in diverse solutions is essential for numerous scientific, pharmaceutical, and technological applications. However, the intricate complexity of protein–protein interactions and their dependence on solution conditions may lead to chemical and physical instability of protein solutions, posing challenges in their processing and target application. Predicting the state of proteins in specific conditions using molecular modelling and theoretical calculations of the second osmotic virial coefficient, which indicates the overall interactions between two macromolecules in a solution, tends to accelerate the discovery of adequate processing conditions and guide experiments. Here, we introduce a new theoretical model called xDLVO-CGhybr to calculate protein solution stability, modulated by diverse protein–protein interactions, by incorporating the most essential interaction potential terms governing protein behaviour. In future applications, this model can be utilised to provide quantitative predictions of protein solubility when coupled with other models that consider protein–solvent interactions. Furthermore, by bridging the gap between macroscopic experimental observables and microscopic structure–function relationships, our research contributes to a deeper understanding of protein behaviour in solution.

## 1. Introduction

Protein–protein interactions (PPIs) in aqueous solution are of great interest from both a fundamental science and a

technology standpoint. Specific protein interactions are typically more directional and greater in magnitude than non-specific interactions. Such specific interactions in living systems, for example, force proteins into biologically relevant assemblies, which provide a distinct biochemical function than for the molecule in the monomer state.<sup>1</sup> In addition, such interactions are responsible for particular recognition, such as substrate to enzyme binding, antigen to antibody binding, or enzyme inactivation.<sup>2</sup>

*Institute of Nanotechnology, Karlsruhe Institute of Technology (KIT), Hermann-von-Helmholtz-Platz 1, 76344 Eggenstein-Leopoldshafen, Germany.*

E-mail: [mariana.kozlowska@kit.edu](mailto:mariana.kozlowska@kit.edu)

† Electronic supplementary information (ESI) available. See DOI: <https://doi.org/10.1039/d3me00086a>



On the other hand, weaker, nonspecific interactions play a crucial role in determining the state of proteins in solution, therefore, they determine the protein's solubility and its tendency to undergo transient aggregation or precipitation. Protein aggregation is a significant issue for the biopharmaceutical industry from a technological standpoint,<sup>3</sup> and it continues to be one of the barriers to the development of biotherapeutics. In general, it is essential to know how to minimise and restrict protein aggregation in specific conditions. Therefore, understanding protein–protein interactions and their dependencies upon the change of solution conditions is essential for designing and developing effective strategies to control protein stability and prevent undesirable aggregation or precipitation. This can significantly impact the performance and shelf-life of protein-based products.<sup>4,5</sup>

To understand conditions that lead to protein aggregation,<sup>6,7</sup> assembly, gel formation or protein crystallisation,<sup>8,9</sup> it is necessary to comprehend forces that act between proteins on a molecular level.<sup>10</sup> Nonspecific interactions are mostly governed by weak noncovalent interactions, such as attractive van der Waals and hydrophobic interactions, and attractive or repulsive short- and long-range electrostatic interactions. The stability of protein solutions is determined by the balance between repulsive and attractive forces, therefore understanding of these interactions on a quantitative level is an important step towards prediction of processability conditions.

The second osmotic virial coefficient,  $B_{22}$ , serves as a valuable indicator of the overall interactions between two macromolecules in a solution,<sup>11</sup> as well as a measure of weak, nonspecific interactions.<sup>12</sup> The  $B_{22}$  coefficient is defined by the deviation of the solution from ideal behaviour and quantifies the extent to which the osmotic pressure differs from that of an ideal solution:

$$\Pi = RTc_p \left( \frac{1}{M_w} + B_{22}c_p + \dots \right), \quad (1)$$

where  $\Pi$  is the osmotic pressure,  $c_p$  is the protein concentration (in mass units),  $R$  is the gas constant,  $T$  is the temperature in K and  $M_w$  is the molecular weight of the protein. Positive values of the coefficient indicate overall repulsive interactions between proteins in solution, while negative values indicate attractive interactions. In diluted protein systems, higher order virial coefficients can be neglected,<sup>13</sup> and therefore the second osmotic virial coefficient provides information on the average effective interaction between macromolecules in solution.

In addition to its theoretical significance, the experimental determination of the second osmotic virial coefficient provides a valuable source for weak PPIs. This technique has been widely employed by researchers to semi-quantitatively predict or explain various thermodynamic properties, including protein solubility,<sup>14–16</sup> crystallisation,<sup>17,18</sup> aggregation propensity,<sup>19</sup> and the critical temperature for liquid–liquid phase separation.<sup>20</sup> As such, the second

osmotic virial coefficient serves as a versatile tool for understanding the behaviour of macromolecules in solution and has become an indispensable part of the modern biotechnology toolkit.<sup>21</sup> In their pioneering work, George and Wilson demonstrated that the measured second osmotic virial coefficients could be correlated to crystallisation behaviour.<sup>17,22</sup> It needs to fall within a narrow interval known as the “crystallisation slot” for protein crystals to be formed. If the values are below the crystallisation slot (indicating stronger attraction), amorphous precipitates would form instead. Since then, the second osmotic virial coefficient has been also used to understand protein solubility at different concentrations and solution conditions. Here, solubility of macromolecules or particles can be modelled using either the thermodynamic relationship between solubility and second osmotic virial coefficients,<sup>14,18</sup> or through semi-empirical models, in which adjustable parameters are fitted from experimental data.<sup>15,16</sup>

Various experimental techniques can be used to measure second osmotic virial coefficients, including membrane osmometry,<sup>12,23</sup> self interaction chromatography,<sup>7</sup> dynamic or static light scattering,<sup>24–27</sup> sedimentation equilibrium, and small angle X-ray or neutron scattering (SAXS/SANS).<sup>28,29</sup> However, these techniques have limitations, as they can be time-consuming or require large amounts of protein samples, making them unsuitable for quick screening of PPIs under various solution conditions. Furthermore,  $B_{22}$  measurements can yield different results when different experimental techniques are used, or even when the same technique is applied by different researchers. Finally, experimentally determined  $B_{22}$  values do not provide information about the origin of PPIs or which molecular interactions contribute the most to the observed macroscopic effects. In addition,  $B_{22}$  was reported also to be calculated using all-atom or coarse-grained molecular dynamics with explicit solvent, *via* free energy techniques.<sup>30</sup> However, the  $B_{22}$  coefficients obtained differ significantly from experimental results. To achieve better agreement with experiments in this case, Lennard-Jones interactions needed to be weakened by a factor of approximately 0.1.<sup>11,30</sup>

The importance of developing theoretical models to rapidly evaluate PPIs under a broad range of solution conditions is evident. Second osmotic coefficients can be derived using concepts of statistical thermodynamics,<sup>13</sup> where  $B_{22}$  is defined as an integral measure of the pair interaction potential  $W(r)$  experienced by particles in solution:

$$B_{22} = \frac{1}{2} \frac{N_A}{M^2} \int_{\Omega_1} \int_{\Omega_2} \int_0^\infty \left( 1 - e^{-\frac{W(r, \Omega_1, d\Omega_2)}{k_B T}} \right) 4\pi r^2 dr d\Omega_1 d\Omega_2 \quad (2)$$

with  $\Omega_1$  and  $\Omega_2$  representing angular orientation, and  $r$  representing centre-of-mass (COM) distance between two proteins with respect to each other. By determining the potential of mean force (PMF) between two macromolecules and integrating it over all relative protein orientations and separations, this equation establishes a relationship between



$B_{22}$  and the effective pair potential. Hence, it offers a method for calculating the effective pair potential.

Various computational methods have been employed to calculate  $B_{22}$  values. For example, Monte Carlo simulations<sup>31</sup> have been used to integrate the Mayer f-function (equal to the negative of the term in brackets in eqn (2)) in the six-dimensional relative configurational space.<sup>32,33</sup> Molecular dynamics,<sup>30</sup> Brownian dynamics<sup>34,35</sup> and Monte Carlo simulations<sup>36</sup> have been used to simulate dilute protein solutions to obtain the radial distribution function (RDF),<sup>34,35</sup> which can be used to determine the Mayer function through the relationship  $\text{RDF}-1 = \text{f-function}$ . Additionally, the PMF has been determined by counting configurations in which proteins interact or by using free energy techniques.<sup>30,37</sup> In these calculations, proteins were modelled using either sphere models,<sup>38,39</sup> coarse grained (CG) models,<sup>30,33</sup> or full all-atom representations,<sup>11</sup> while the solvent was mostly represented implicitly. Some researchers have also focused on optimising the force field by tuning the nonbonded parameters to match the experimentally determined  $B_{22}$  values.<sup>30</sup> Aside from the aforementioned computationally expensive methods, there are also simplified models available for calculating second osmotic virial coefficients, where proteins are represented as spheres. One widely used model is based on the colloidal DLVO (Derjaguin–Landau–Verwey–Overbeek) theory,<sup>40</sup> which describes the interaction between proteins as a combination of spherically symmetric van der Waals forces and repulsive electrostatic interactions between charged macroions surrounded by small ions:

$$W(r) = W_{\text{disp}}(r) + W_{\text{el}}(r). \quad (3)$$

The DLVO model is widely used to interpret experimental data, such as salt dependence on  $B_{22}$ .<sup>16,41</sup> However, the parameters derived from such applications often lack physical significance or are poorly transferable to other proteins or solvent conditions. Some modifications of the DLVO theory, such as the inclusion of other potential terms, like the osmotic depletion potential,<sup>12,15</sup> potential that models hydrophobic forces, or potential terms that describe the effects of excipients or polymers,<sup>42,43</sup> have been reported. Despite these efforts, fundamental limitations of the DLVO theory persist, *i.e.* it agrees well with experiments conducted only on the spherical particles.<sup>16</sup> Moreover, proteins can experience various non-DLVO interactions, including hydrodynamic and solvation forces or can exist in various non-spherical forms, which can significantly impact the quality of the prediction. Therefore, while the DLVO model is a useful tool, it is crucial to consider its limitations and other contributing factors to better understand protein behaviour and PPIs.

Among protein–protein interactions, electrostatic interactions are particularly important, as the protonation states of amino acids are pH-dependent and can vary based on the local protein environment. Moreover, proteins come

in a range of shapes and can exhibit significant charge anisotropy, which can impact their physicochemical properties. As a result, the behaviour of proteins in solution is influenced by a variety of solution conditions, modulating to a huge extent the electrostatic PPIs. It includes solution pH, ionic strength, and the addition of polyelectrolytes or small molecule additives. One common approach for modulating PPIs in solution is to adjust the salt concentration, which weakens repulsive electrostatic interactions. In addition, according to the Lifshitz theory of electrodynamic forces,<sup>44,45</sup> changing the ionic strength can also have an impact on dispersion interactions, with some estimates suggesting a change of around 10% at high ionic strengths.<sup>41</sup> However, including the effects of ionic strength on dispersion interactions is challenging, and therefore, in the majority of theoretical models dispersion interactions are assumed to be independent of ionic strength.

Most theoretical models to calculate  $B_{22}$  values use simplified continuum models to simulate electrostatic interactions. They are mainly based on Debye–Hückel theory. However, DH theory is an approximation, especially valid for diluted solutions at low ionic strengths (*e.g.* of 0.1 M), and has not been extensively tested for its validity in representing biomolecular electrostatics. Some attempts have been made to move beyond Debye–Hückel theory. Kim *et al.* have used a fast multipole method solved by a boundary element method to model electrostatic interactions at a residue-level coarse-grained structure.<sup>46</sup> Song *et al.* have proposed the extended Debye–Hückel continuum model to improve solvation dynamics.<sup>47</sup> In addition, Neal *et al.* have used Poisson–Boltzmann theory to solve the electrostatic potential between atomistically represented proteins to compute  $B_{22}$ .<sup>11</sup> The PB equation is a partial differential equation that describes the electrostatic potential and ion distribution around charged molecules or macromolecules in an electrolyte solution.<sup>48</sup> It takes into account the charges on a molecule, the dielectric constant of the solvent, and the concentration of ions in the solution. It is a popular approach for calculating the electrostatic interaction of proteins and other biomolecules.<sup>48–51</sup> However, computational cost of PB for macromolecules restricts this method only to a small number of relative protein orientations. In addition, PB theory cannot take into account ion specificity.<sup>53</sup> Therefore, Boström *et al.* have modified the Poisson–Boltzmann method and incorporated ion-specific effects in spherical protein representations.<sup>38,39,52,53</sup>

Recently, we have reported the xDLVO-CG model, which is an approach to compute second osmotic virial coefficients of proteins by adapting the equations of extended DLVO (xDLVO) theory for the use on coarse-grained protein structures.<sup>54</sup> While the xDLVO-CG model showed reasonable agreement with experimental values for  $B_{22}$  coefficients, some discrepancies were observed for large and irregularly-shaped proteins, such as bovine serum albumin and monoclonal antibodies. While computationally efficient, we have found that this approach may not capture molecular-level details on



short protein–protein distances, accounted for in the higher resolution (computationally expensive) models.

To improve accuracy of xDLVO-CG and better model complex biological systems, we report here the xDLVO-CGhybr model, which includes modified electrostatic potential term. The xDLVO-CGhybr model employs a hybrid approach that combines Poisson–Boltzmann theory and Debye–Hückel theory to calculate the electrostatic contribution to the total interaction potential, regardless of protein size and shape. Given the computational complexity of solving PB equations for protein systems, particularly when determining second osmotic virial coefficients for diverse starting orientations, COM distances, and salt concentrations, we chose a hybrid approach. This strategy effectively balances computational efficiency and accuracy. Additionally, in the present report we also implemented a coarse-grained-based Lennard-Jones potential that is carefully parameterized to match reference all-atom potentials for accurate prediction of dispersion-based PPIs. To validate the accuracy of our model, we tested it on six different proteins with varying complexity and shape: bovine trypsin inhibitor (BPTI), ribonuclease A (RbnA), chymotrypsinogen (ChmT), concanavalin A (ConcA), bovine serum albumin (BSA) and human immunoglobulin type I (IgG1). The new implementation demonstrates improved predictions of  $B_{22}$  values at ionic strength of 10 mM to 1 M and arbitrary pH.

## 2. Theoretical background

### 2.1. Interaction potential in xDLVO-CGhybr model

In the xDLVO-CGhybr model, the interaction potential, denoted as  $W(r)$ , is computed by summing up the electrostatic,  $W_{\text{el}}(r)$ , dispersion,  $W_{\text{disp}}(r)$ , osmotic,  $W_{\text{osm}}(r)$ , and ion-protein,  $W_{\text{i-pr}}(r)$  potential terms between pairs of proteins. The resulting equation for the interaction potential is:

$$W(r) = W_{\text{el}}(r) + W_{\text{disp}}(r) + W_{\text{osm}}(r) + W_{\text{i-pr}}(r). \quad (4)$$

Therefore, it consists of similar four terms as were implemented in the previously reported xDLVO-CG model,<sup>54</sup> but electrostatic and dispersion potentials are modified in xDLVO-CGhybr. These modifications are explained in detail below. The osmotic attraction and ion-protein potential terms remained unchanged, so we explain them only briefly.  $W_{\text{osm}}(r)$  arises from the exclusion of salt ions between proteins at short distances. It leads to a local osmotic pressure imbalance compensated by an attractive interaction between the proteins.<sup>55</sup> In the model implemented (also in our previous work), this potential considers the mean hydrated radius of salt and the salt density. The ion-protein dispersion potential involves the total dispersion interaction between a protein and the ions in its vicinity. The calculation includes parameters characterising the dispersion interaction between the protein and anion and cation ions, respectively. For a more thorough explanation of these terms and

respective equations, please refer to our previous publications.<sup>12,54</sup>

### 2.2. Electrostatic interactions

The xDLVO-CGhybr model employs a hybrid approach to calculate the electrostatic interaction energy between two proteins. At short protein separations, *i.e.* up to  $R_0 + 2$  nm, where  $R_0$  represents the COM distance between proteins in their crystal structure, the model uses the Poisson–Boltzmann equation and all-atom protein structures to compute electrostatic interaction energy ( $E_{\text{PB}}$ ). At larger distances, the Debye–Hückel model and coarse-grained protein structures are used instead ( $E_{\text{DB}}$ ):

$$W_{\text{el}}(r) = \begin{cases} E_{\text{PB}}(r), & r \leq R_0 + 2 \text{ nm} \\ E_{\text{DB}}(r), & r > R_0 + 2 \text{ nm} \end{cases} \quad (5)$$

This scheme is illustrated in Fig. 1.

In contrast, xDLVO-CG is a purely coarse-grained model that calculates all potential terms, including the electrostatic interaction energy, using simplified shape-based CG representations without the use of the hybrid resolution, as we implemented in xDLVO-CGhybr.

The linearized Poisson–Boltzmann equation can be expressed using the following formula:<sup>51</sup>

$$-\Delta \cdot \epsilon(x) \Delta \phi(x) + \kappa^{-2} \phi(x) = \frac{4\pi e^2}{k_{\text{B}} T} \sum_{i=1}^M q_i \delta(x - x_i), \quad (6)$$

for  $x \in \Omega$ , where  $\phi(x) = g(x)$  for  $x \in \partial\Omega$

This equation solves for the dimensionless electrostatic potential  $\phi(x)$ , resulting from a charge distribution in a polarizable continuum with dielectric constant  $\epsilon(x)$ , within a finite domain  $\Omega$  with Dirichlet boundary conditions, where  $g(x)$  represents a fixed potential on the boundary. In general, in a biomolecular system exist two types of charges: fixed charges ( $q_i$  with coordinates  $x_i$ ), which are associated with proteins (represented on the right side of eqn (6)), and mobile charges, which represent the counterions present in the surrounding electrolyte (shown in the second term on the

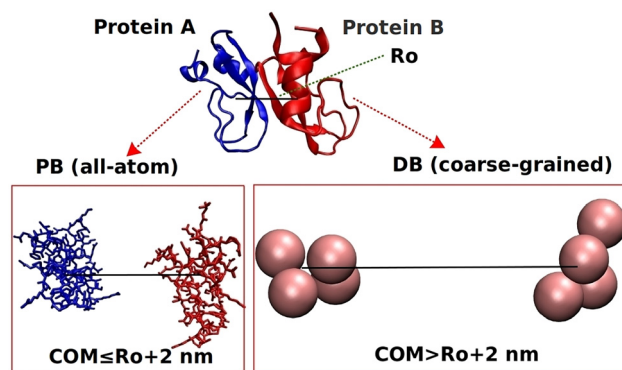


Fig. 1 Illustration of hybrid (all-atom and coarse-grained) scheme used to calculate electrostatic interactions between proteins in xDLVO-CGhybr model.





left side of eqn (6)). There,  $\kappa$  denotes the coefficient which describes ion accessibilities and ionic strength.<sup>49,50</sup> After solving the PB equation to determine the electrostatic potential  $\phi(x)$ , the free energy,  $G(\phi)$ , can be calculated by integrating the potential across the relevant domain:<sup>50</sup>

$$G(\phi) = \int_{\Omega} \left[ \rho_f \phi - \frac{\epsilon}{2} (\Delta \phi)^2 - \kappa^{-2} (\cosh \phi - 1) \right] dx. \quad (7)$$

In eqn (7), the first term corresponds to the energy required to insert the protein charges into the electrostatic potential, which can be seen as the energy of interaction between the fixed charges. The second term represents the energy of polarisation in the dielectric medium. Lastly, the third term takes into account the energy of the mobile charge distribution, which can be interpreted as the excess osmotic pressure of the system. Since the PB equation cannot be solved analytically, we have employed a numerical method, *i.e.* the finite difference method.

In xDLVO-CGhybr, when proteins are located in close proximity to each other, the electrostatic interaction energy,  $E_{PB}(r)$ , is obtained by calculating several energy terms and their difference shown in eqn (8). Therefore,  $E_{PB}(r)$  is the difference between the total electrostatic free energy of the protein complex and the electrostatic energies of the individual, separated proteins:

$$E_{PB}(r) = G_{\text{complex}}(r) - G_{\text{Prot1}}(r) - G_{\text{Prot2}}(r), \quad (8)$$

where the term  $G_{\text{complex}}$ ,  $G_{\text{Prot1}}$  and  $G_{\text{Prot2}}$  represent the electrostatic free energy obtained through the use of an iterative solver.<sup>48</sup>

When the protein separation exceeds  $R_0 + 2$  nm, electrostatic interactions are computed using the computationally less expensive Debye–Hückel model as follows:

$$W_{\text{el}}(r) = \sum_{i=1}^{N_1} \sum_{j=1}^{N_2} \frac{Z_i Z_j e^2 \exp(\kappa(R_{bi} + R_{bj} - r_{ij}))}{4\pi\epsilon_0\epsilon_r r \left(1 + \frac{\kappa(R_{bi} + R_{bj})}{4}\right)^2}, \quad r_{ij} > d_{ij} + 2\sigma, \quad (9)$$

where  $R_{bi}$  and  $R_{bj}$  represent bead radii assumed to be equivalent to the radius of gyration of the constituent atoms.  $N_1$  and  $N_2$  denote the total number of beads,  $d_{ij}$  is the initial distance between bead pairs,  $r_{ij}$  corresponds to the current bead-to-bead distance during protein translation,  $\sigma$  is the thickness of the water layer surrounding the protein (0.1 nm),  $r$  represents the relative permittivity,  $Z_i$  and  $Z_j$  indicate the charges of the beads, and  $\kappa$  is the reciprocal of the Debye length, which is given by:

$$\kappa = \sqrt{\frac{2N_A e^2 I}{\epsilon_0 \epsilon_r k_B T}}, \quad (10)$$

where  $I$  stands for ionic strength,  $N_A$  stands for Avogadro number,  $k_B$  stands for Boltzmann constant, and  $T$  stands for absolute temperature.

### 2.3. The dispersion potential

In the xDLVO-CGhybr model, the dispersion interactions between proteins are calculated through either the Hamaker potential or the Lennard-Jones potential. The Hamaker potential describes the attraction forces between molecules arising from electromagnetic quantum fluctuations.<sup>44,45,56</sup> It is derived by integrating the London dispersion forces, between two homogeneous spheres,<sup>57</sup> and is represented by following equation:

$$W_H(r) = - \sum_{i=1}^{N_1} \sum_{j=1}^{N_2} \frac{A_H}{12 N_1 N_2} \frac{1}{r_{ij}^2 - d_{ij}^2} \left[ \frac{d_{ij}}{r_{ij}^2 - d_{ij}^2} + \frac{d_{ij}^2}{r_{ij}^2} + 2 \ln \left( 1 - \frac{d_{ij}^2}{r_{ij}^2} \right) \right], \quad r_{ij} > d_{ij} + 2\sigma \quad (11)$$

The Hamaker constant is represented by  $A_H$  in the formula. It determines the depth of the interactions between the two surfaces and is the only adjustable parameter in the model. The value of  $A_H$  depends on various factors, such as the dielectric polarizability of macromolecules and of the surrounding medium, the separation distance between the two surfaces, and the properties of the interacting surfaces themselves.<sup>58</sup>

Furthermore, the dispersion interactions between proteins were also calculated based on the Lennard-Jones potential, represented by following equation:

$$W_{LJ}(r) = \sum_{i=1}^{N_1} \sum_{j=1}^{N_2} \epsilon_{ij} \left[ \left( \frac{\sigma_{ij}}{r_{ij}} \right)^{12} - \left( \frac{\sigma_{ij}}{r_{ij}} \right)^6 \right], \quad r_{ij} > d_{ij} + 2\sigma. \quad (12)$$

Here,  $\epsilon_{ij}$  and  $\sigma_{ij}$  represent the respective Lennard-Jones parameters for each bead pair. They were directly parametrized from all-atom LJ potentials (as described in Computational details) unlike the Lennard-Jones parameters in our previous work,<sup>54</sup> which were derived using a simplified method implemented in the coarse-grained builder in VMD (shape-based CG).<sup>59</sup>

## 3. Computational details

### 3.1. Preparation of protein structures

The all-atom structures of proteins were taken from the protein data bank (PDB) with the codes 1bpi, 3rn3, 2cga, 3nwk, 4f5s and 1mco for bovine BPTI, Rbna, ChmT, Conca, BSA and IgG1, respectively. The chosen PDB structures were checked if they contain the missing residues, and in case they did, they were reconstructed by the Swiss Model program.<sup>56</sup> The protonation states of protein residues were assigned at desired pH (see in Results and Discussion) by using PROPKA method (version 3.3)<sup>48,60</sup> and PDB2PQR online web server.<sup>61</sup> Such starting all-atom structures of proteins were used for the PB calculation with Adaptive Poisson–Boltzmann Solver (APBS)<sup>60</sup> on short distances (described in section 3.2), where partial charges and van der Waals radii were assigned to the atoms using the CHARMM force field.<sup>62</sup> The protonated all-atom structures were also used for the CG mapping (with approximately 500 atoms per one bead) for all



other calculations for the intermolecular distances higher than  $R_0 + 2$  nm, as depicted in Fig. 1. CG mapping was performed by using a shape-based coarse-grained model,<sup>59</sup> implemented in the VMD program (version 1.9.3).<sup>63</sup> Center of each bead was placed in the COM of the corresponding atoms. The bead radius was assigned to the radius of gyration, whereas the charge of the bead was calculated as a sum of partial charges of all atoms comprising the bead. Upon CG mapping of BPTI and RbnA, each protein unit was represented by 4 beads, while ChmT, ConcA, BSA, and IgG1 were represented by 8, 15, 20, and 40 beads, respectively (see Fig. S1†).

### 3.2. Poisson–Boltzmann calculations

Adaptive Poisson–Boltzmann Solver (APBS) was used to conduct Poisson–Boltzmann calculations on all-atom protein structures studied.<sup>48,60</sup> Specifically, it was used to solve the linearized finite difference Poisson–Boltzmann equation (lpbe). The iterative solver was initially applied on coarse grid dimensions with fewer grid points and larger size, obtained by expanding the molecular dimensions by a factor of 1.7. Subsequently, the resulting Dirichlet boundary conditions were utilised to solve the equation on a smaller region of interest using a finer grid, obtained by increasing the molecular dimensions by 20 Å. For lpbe calculations of each protein, the number of grid points, the dimensions of the coarse grid and of the fine mesh domain were set by the internal APBS script. To obtain the electrostatic binding energy of the protein complex for a specific COM distance or ionic strength, six lpbe calculations were required: two for the complex and two for each protein. These calculations were performed with the same grid spacing to ensure proper cancellation of self-solvation energies. The electrostatic interaction energy was then calculated as the difference between the electrostatic energy of the complex and the electrostatic energies of the separated proteins. APBS calculations were carried out at 20 different monovalent salt concentrations ranging from 10 mM to 1 M NaCl. Specifically, concentrations were incremented by 27 mM up to 0.2 M, and by 70 mM for concentrations exceeding 0.2 M. The sodium and chloride radii were set to 2.0 Å and 2.23 Å, respectively. For each calculation at specific salt concentration, one of the proteins was kept fixed in space, while another protein was translated along the vector connecting their COMs, by incrementing the distance by 1 Å in each step. The second protein was moved up to a distance of  $R_0 + 2$  nm from its starting COM distance  $R_0$ , and APBS calculations were performed at each intermediate distance (in total 120 lpbe calculations for one concentration).

Multiple Debye–Hückel boundary conditions were employed, and the molecular surface was smoothed using 9-point harmonic averaging<sup>64</sup> with the solvent (water) probe radius set to 1.4 Å and the solvent density set to 10 quadrature points per Å.<sup>2</sup> The cubic B-spline discretization was used to map protein charges to the grid. The internal

dielectric constant of all proteins studied was set to 4.0, while the external dielectric constant was set to 78.4 (the dielectric constant of water medium).

### 3.3. LJ parameters for CG model

The CG beads, obtained with procedure explained in section 3.1, were assigned  $R_{\min}$  values equal to the radius of gyration of their constituent atoms. The sigma parameter in the LJ potential was set as  $R_{\min} = 2^{1/6}\sigma$ , and the epsilon parameters were adjusted to match the all-atom LJ potential. The all-atom LJ potential was obtained by using CHARMM36m parameters calculated on a translation trajectory created by translating proteins over vectors between COMs of protein pairs from five different relative orientations.<sup>62,65</sup> The CG LJ potential was fitted to the all-atom potential by varying epsilon parameters using a least squares algorithm. The interaction parameters between different beads were determined using Lorentz–Berthelot combining rules.

Finally, the depth of the CG LJ potential was scaled to match the Hamaker dispersion potential, as LJ parameters are usually optimised for vacuum and have a weaker effective interaction in a solvent.<sup>30,66,67</sup> For that, we have used either  $A_H$  values reported in the literature (see Table S1†) or assigned a general value of  $5 k_B T$ , *i.e.* according to fundamental Lifshitz theory of electrodynamic forces.<sup>44,45</sup> Such value is characteristic to a variety of proteins. The list of parameters used for LJ scaling is given in Table S1 in the ESI.† We have to point out that the only adjustable parameter in our model is the Hamaker constant for each of the proteins (see eqn (11)).

### 3.4. Calculations of second osmotic virial coefficients

PMF was calculated by summing interactions between the corresponding bead pairs from each protein pair, according to eqn (4)–(12). The PMF and  $B_{22}$  were calculated by the in-house code, and  $B_{22}$  was determined by numerical integration of the PMF over different protein–protein orientations according to eqn (2). Protein–protein orientations were sampled by the procedure described in our previous work,<sup>54</sup> except that due to higher computational cost of PB calculations at short COM distances, PMF was determined over less protein–protein configurations, *i.e.* by starting from 83 starting radial positions. For each starting configuration the PMF was calculated by translating proteins over vector connecting COMs of two protein pairs, up to a distance of  $R_0 + 30$  nm, where  $R_0$  is the initial distance.

Additionally, to enable a comprehensive comparison of xDLVO-CGhybr with other models, we also calculated  $B_{22}$  values using our previously reported xDLVO-CG model,<sup>54</sup> spherical xDLVO model<sup>16,41</sup> and an all-atom FMAPB2 model.<sup>66</sup> The FMAPB2 uses an all-atom protein representation in combination with an implicit solvent model and is publicly available on a web server (<https://pipe.rcc.fsu.edu/fmapb2/>). For xDLVO calculations, the protein charge was set to be equal to the charge obtained by PROPKA, and



the protein radius was set to be equal to the experimentally determined hydrodynamic radius from the literature.

## 4. Results and discussion

To validate our model, we performed calculations on six diverse proteins: BPTI, RbnA, ChmT, ConcA, BSA, and IgG1. These proteins vary in size and shape, ranging from small and intermediate (BPTI, RbnA and ChmT with 58aa, 124aa and 395aa, respectively) to large (ConcA, BSA and IgG1 with 474aa, 583aa and 1287aa, respectively) proteins. Moreover, they represent either simple spherical or ellipsoidal to more irregular shapes. The structure and shape of the six proteins studied are shown in Fig. 2, along with their corresponding electrostatic maps. From the visualisation of the electrostatic maps one can notice that the proteins selected possess

various degrees of positive (in blue) and negative (in red) charge localization. Some proteins in the pH given show less charge anisotropy (e.g. RbnA, Fig. 2b), while in most cases proteins possess larger differences in the surface charges.

Given the diverse characteristics of these six proteins in terms of their size and shape, as well as the availability of experimentally measured data for their second osmotic virial coefficients, we regard this dataset as a suitable basis for validating the accuracy and applicability of the xDLVO-CGhybr model. We compared the calculated results to the experimental  $B_{22}$  values reported in the literature. The results section is organised as follows: first, we discuss the impact of employing the hybrid Poisson–Boltzmann/Debye–Hückel scheme and the criteria for switching between models. Next, we present  $B_{22}$  calculations with the new method developed and validate results in comparison with experimental data and other models. In the end, we briefly discuss the impact of including Lennard-Jones interactions versus Hamaker dispersion potential on the accuracy of calculations.

### 4.1. Poisson–Boltzmann and Debye–Hückel approaches in xDLVO-CGhybr

In this study, we aimed to improve the accuracy of the electrostatic part of the PMF reported in xDLVO-CG by using a hybrid approach based on Poisson–Boltzmann and Debye–Hückel theory. Specifically, we employed PB calculations on all-atom structures at short COM distances, and Debye–Hückel calculations on coarse-grained structures at larger COM distances, as depicted in Fig. 1. To demonstrate criteria used for the linking of two different methods, the comparison of the electrostatic energy term of interactions between two different proteins: BPTI and IgG1 using PB and DH has been performed, as illustrated in Fig. 3. The results are plotted as a function of the COM distance between the two proteins and the vertical dashed orange line indicates the point at which the electrostatic potential in the xDLVO-CGhybr model switches from PB to DH.

The analysis of IgG1 and BPTI revealed that the largest differences are observed at short COM distances, *i.e.* around 2 nm from the position of the proteins in their crystal structure. Note that the COM between BPTI and IgG1 in the crystal is 2.41 nm and 7 nm, respectively. The energies are fairly similar at larger protein separations. This indicates that DH theory cannot properly describe repulsion interactions between proteins on shorter distances. At these distances, repulsion energy obtained by using the Debye–Hückel model is generally smaller than those obtained by PB theory, *i.e.* by a factor of three to five or more. This conclusion applies to all proteins studied (see Fig. S2†). A smooth transition from PB to Debye–Hückel potential was observed at intermediate COM distances that are on average of  $R_0 + 2$  nm. For this reason, we implemented different integration schemes that switch at this distance. The Debye–Hückel equation is an analytical solution of the PB

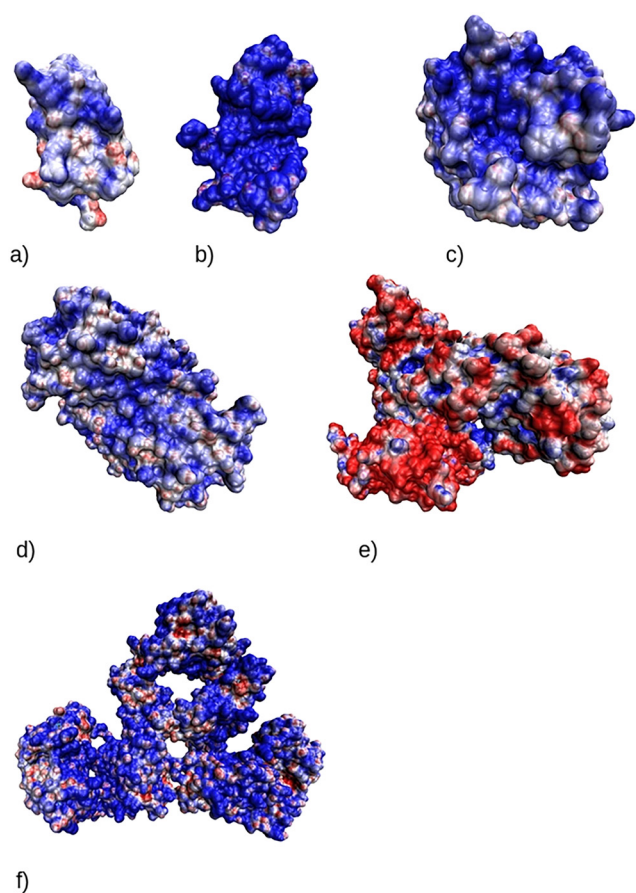


**Fig. 2** The visualisation of the structure and electrostatic maps of six proteins studied in the present work: a) bovine trypsin inhibitor (BPTI) at pH 4.9 (total charge of +6), b) ribonuclease A (RbnA) at pH 3 (total charge of +16), c) chymotrypsinogen (ChmT) at pH 3 (total charge of +17), d) concanavalin A (ConcA) at pH 4 (total charge of +25), e) bovine serum albumin (BSA) at pH 7.4 (total charge of -16), and f) human immunoglobulin type 1 (IgG1) at pH 6.5 (total charge of +27). The protein surface is coloured according to the electrostatic potential calculated by APBS, with blue, red and white colours indicating regions of excess positive, negative and neutral charges respectively. The sizes of the proteins in the illustrations are not to scale, but are depicted for viewer convenience.





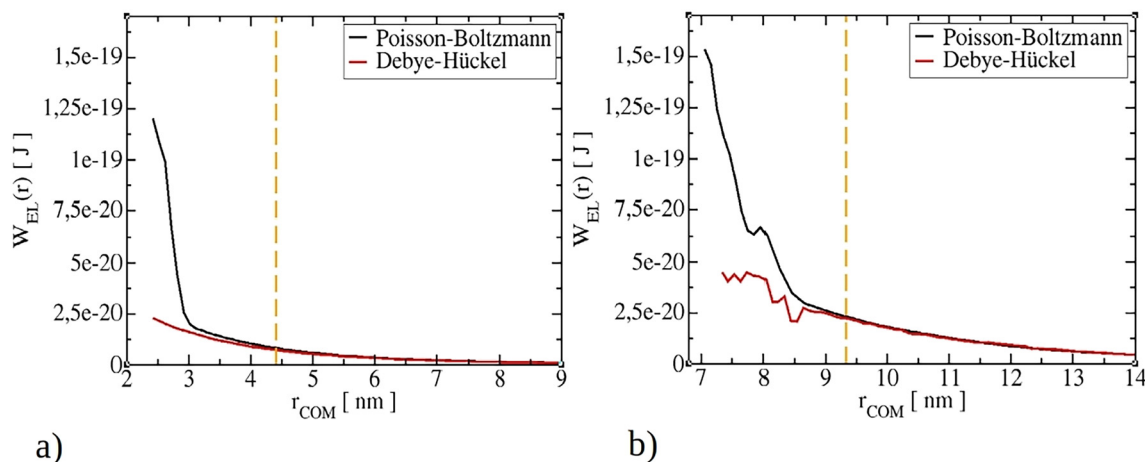


**Fig. 3** Comparison of calculated energy of electrostatic interactions at 10 mM NaCl between a) two BPTI and b) two IgG1 proteins by solving Poisson–Boltzmann equations (applied to the full all-atom structure of proteins) and by using Debye–Hückel theory (applied to the coarse-grained model of proteins). The vertical dashed orange line indicates the COM distance (at  $R_0 + 2$  nm), where electrostatic potential in xDLVO-CGhybr is switched from Poisson–Boltzmann to Debye–Hückel model.

equation for interaction between two homogeneously charged spheres of equal radius. It gets more approximative, while using it for other cases.

The larger deviation between these two models at short separations is expected because specific (local) residue–residue interactions can be better described by all-atom protein representation and PB theory. At the protein–protein interface, the effective dielectric constant can shift from the solvent to the protein interior. As a result, these residues effectively interact as if they belong to the same protein within its low dielectric environment. This results in a higher repulsive charge–charge interaction than if they were placed in a solvent medium. As the protein–protein separation increases, residues become more solvated, thus beginning to feel the dielectric environment of the solvent, reducing repulsion.<sup>68</sup> The effects of dielectric discontinuity become significant only at separations less than Debye length.

The PB numerical methods determine the dielectric constant by rolling a solvent sphere with its probe radius over the protein surface, which distinguishes the solvent region from the protein interior region, each having a different dielectric constant. Therefore, the electrostatic interactions between proteins depend greatly on their unique shape and charge distribution. The energy of polarisation, arising from the dielectric interface (as described in the second term of eqn (7)), is affected mostly by partial atomic charges located near the surface. These factors, along with others, contribute significantly to the interaction energy and are better described by PB theory<sup>49</sup> than by DH. We found that the new hybrid approach in xDLVO-CGhybr provides fairly accurate modelling of electrostatic effects, which should lead to better agreement of second osmotic coefficients in comparison to experiments in comparison to previously reported methods.

#### 4.2. Calculation of $B_{22}$ coefficients for small sized proteins

**Bovine pancreatic trypsin inhibitor.** BPTI is a small ellipsoid-shaped protein that consists of 58 residues and has a molecular mass of 6.5 kDa. It binds with high affinity to trypsin and other digestive proteases, inhibiting their enzymatic activity.<sup>69</sup> Trypsin inhibitors naturally found in various plants, including soybeans, legumes, and grains, where it acts as a self-defence mechanism.<sup>69</sup>

Fig. 4b presents the calculated  $B_{22}$  coefficients for BPTI at pH 4.9 using xDLVO-CGhybr, in comparison to xDLVO-CG, FMAPB2, and xDLVO models. The calculated values at low and medium salt concentrations decrease faster towards negative values of  $B_{22}$  (*i.e.* stronger attractive interactions) with increasing ionic strength using xDLVO and xDLVO-CG methods. Theoretically determined  $B_{22}$  data points, derived using the xDLVO-CGhybr model, cross zero at approximately 0.42 M, following a similar trend to the experimental data. Calculated values of  $B_{22}$  coefficients show nearly quantitative agreement with experimental results of Farnum *et al.*, who performed static light experiments to measure the experimental  $B_{22}$  values.<sup>70</sup> To the best of our knowledge, no other experimental  $B_{22}$  measurements were performed on BPTI protein. In comparison, the  $B_{22}$  values obtained using xDLVO-CG are shifted more to the negative values. The zero-crossing point is located at a lower ionic strength of 0.36 M NaCl.  $B_{22}$  values calculated with FMAPB2 correlate with xDLVO-CGhybr results and match with experimental data at most of the points except at the lowest ionic strength of 0.3 M. At this ionic strength, the FMAPB2 model results in a  $B_{22}$  value of  $-2.05 \times 10^{-5} \text{ mol ml g}^{-2}$ , while the experimentally determined value is  $3.32 \times 10^{-4} \text{ mol ml g}^{-2}$ . xDLVO-CGhybr gives a value of  $3.32 \times 10^{-4} \text{ mol ml g}^{-2}$ . Differences between calculations made with these two different methods differ more at lower ionic strengths. Given the lack of available experimental measurements, it is hard to judge which model





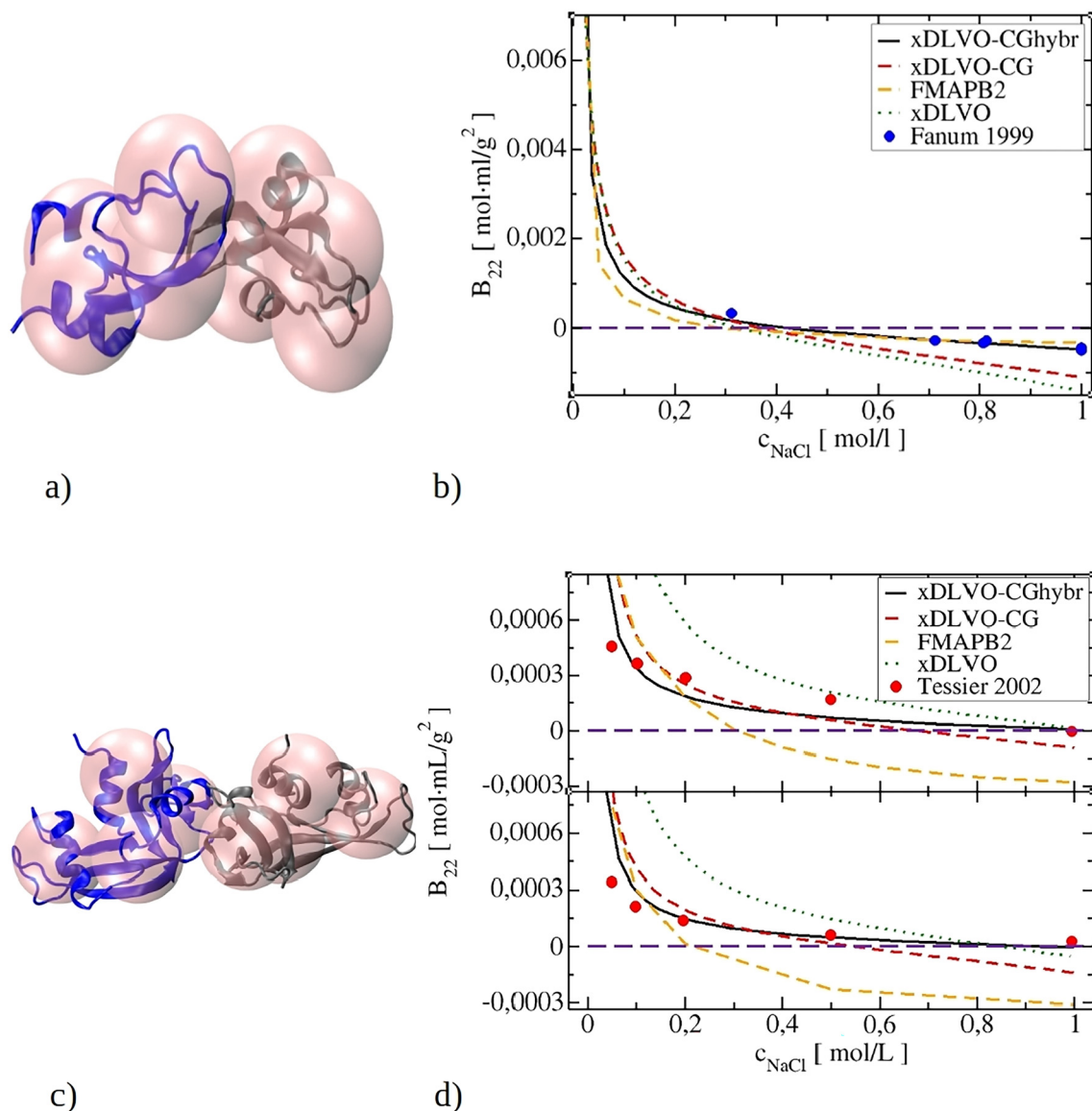


Fig. 4 Visualisation of BPTI (a) and RbnA (c) proteins using the coarse-grained model implemented in xDLVO-CGhybr. The new cartoon representation of all-atom proteins is given for clarity. Calculated  $B_{22}$  coefficients for BPTI at pH 4.9 (b) and RbnA at pH 3 and pH 4 (upper and lower panel) (d) as a function of NaCl concentration.  $B_{22}$  values are compared with the values obtained with xDLVO-CG (dashed red), FMAPB2 (dashed orange) and xDLVO (green dots) models and experimental results (red circles).

performs better at low salt conditions. In general, both xDLVO-CGhybr and FMAPB2 follow experimentally obtained trends better than other methods.

The xDLVO model overestimates the  $B_{22}$  values and is out of range of experimental values except at the first point. From Fig. 2a, we see that at pH 4.9, the protein has a relatively high charge as for its small size (+6 according to the PROPKA method). Fig. S1a† shows that BPTI has mostly positive local charge distribution which contributes to high electrostatic repulsion, necessitating an intermediate salt concentration to screen electrostatic interactions and shift protein–protein interactions from repulsive to attractive ones. This may be the reason for the poorer description of electrostatic PPIs in xDLVO. It should be mentioned that other researchers, such

as Mereghetti *et al.*, have employed also Brownian dynamics simulations to calculate the second osmotic virial coefficients of BPTI solutions.<sup>34</sup> There, they have used an all-atom protein representation, aiming to compute  $B_{22}$  and diffusion coefficients, however they could only achieve a semi-quantitative agreement with experimental data.

**Contribution of potentials in the PMF.** Understanding the trends observed in the changes of the second osmotic virial coefficients requires a detailed examination of the potential of mean force. Fig. 5a highlights how PMF varies with the addition of salt. At low salt concentrations, the PMF shows strong repulsion between the proteins due to electrostatic interactions. Increasing the salt concentration leads to a screening effect that reduces the strength of the repulsive



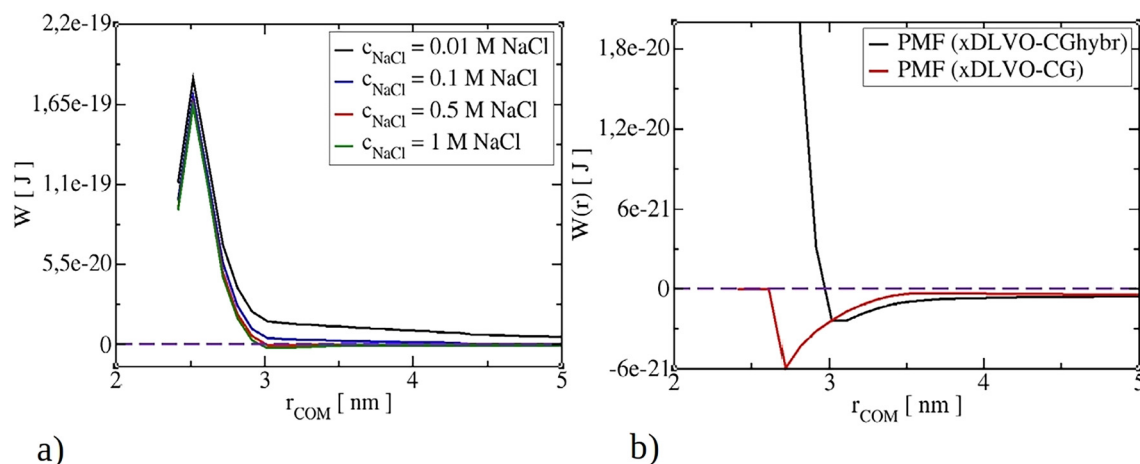


Fig. 5 Changes of the PMF of BPTI at pH 4.9 with increasing NaCl concentration using xDLVO-CGhybr (a). Comparison of the PMF at 1 M NaCl obtained by xDLVO-CGhybr and xDLVO-CG models (b).

interactions. Further increase of ionic strength results in more pronounced dispersion interactions between the proteins. This shift in dominant PPI interactions, *i.e.* from electrostatic to dispersion forces, is due to the charge screening effect that reduces the influence of electrostatic forces, making dispersion forces more important in determining the behaviour of the proteins at higher ionic strengths. In Fig. 5b, the PMF of BPTI at a salt concentration of 1 M NaCl obtained using xDLVO-CGhybr and xDLVO-CG models is illustrated. PB theory indicates repulsive interactions even at 1 M NaCl, however, the respective peak only exists at the first five distances, *i.e.* up to COM of 2.91 nm. Potential in xDLVO-CG shows higher attractive contributions, which explains lower  $B_{22}$  values in Fig. 4b. By examining the PMF carefully, we can gain a better understanding of the underlying PPIs of the system and the factors that contribute to changes in the  $B_{22}$  values.

**Bovine pancreatic ribonuclease.** Ribonuclease A, RbnA, is a digestive enzyme found in the pancreas that plays a critical role in the digestion of single-stranded RNAs in food.<sup>71</sup> This small protein is composed of 124 amino acid residues and has a triangular shape (see Fig. 4b) and a molecular mass of 13.7 kDa. Its ease of purification and small size make it a valuable tool in biochemical research.<sup>71</sup> Fig. 4d displays the calculated  $B_{22}$  coefficients for RbnA at pH 3 and 4 and at ionic strengths ranging from 50 mM to 1 M NaCl. Experimentally determined  $B_{22}$  values at pH 3 are positive in most cases, indicating repulsive PPIs until a concentration of approximately 0.95 M NaCl is used.<sup>72</sup> The values of second osmotic virial coefficients calculated using the xDLVO-CGhybr model follow a similar trend of  $B_{22}$  decrease as a function of ionic strength increase. Since electrostatic forces play a decisive role in this case, the hybrid scheme of treating electrostatics in xDLVO-CGhybr improves the calculated  $B_{22}$  values in comparison to xDLVO-CG. The calculated data match the experimental data in a semi-quantitative manner, with good agreement observed at 0.1 M and 1 M NaCl.

However, experimental data of the  $B_{22}$  decrease at pH 3 is non-monotonous. This trend cannot be fully captured using the coarse-grained protein model in xDLVO-CGhybr and without considering dynamical changes on an all-atom level.

As the ionic strength increases, the repulsion between proteins is diminished due to electrostatic screening, resulting in decrease of  $B_{22}$  coefficients. At the highest salt concentration (1 M NaCl), the experimentally determined  $B_{22}$  value is  $-2.70 \times 10^{-6}$  mol ml  $g^{-2}$ , while the value calculated using the xDLVO-CGhybr model is  $-2.72 \times 10^{-6}$  mol ml  $g^{-2}$ . This shows a good agreement of data and indicates that the  $B_{22}$  coefficient is close to the zero-crossing point. Such a small value of  $B_{22}$  is insufficient to indicate sufficiently strong attractive PPIs, thus aggregation should happen at higher ionic strengths. The  $B_{22}$  values calculated at pH 4 using xDLVO-CGhybr follow a similar trend, but they are slightly shifted towards negative values, *i.e.* more prone aggregation, due to a decrease in protein charge (+16 and +13 at pH 3 and pH 4, respectively). Calculated values of  $B_{22}$  at pH 4 also show repulsive interactions at almost all salt concentrations considered. They agree nearly quantitatively with experimental data, except at the first two points at low ionic strength. From Fig. 4d, it is evident that increasing the ionic strength up to 1 M NaCl is not sufficient to shift PPIs in RbnA towards attraction since  $B_{22}$  does not cross the zero-point. The reason behind the repulsive interactions in this case is the high protein charge of RbnA, despite its small size. The distribution of positive charges throughout the protein is uniform (see Fig. S1b†), without any significant charge anisotropy that can reduce the electrostatic repulsion.

In comparison to the xDLVO-CGhybr,  $B_{22}$  values obtained from the xDLVO-CG model are slightly higher at low salt concentrations (below 0.3 M NaCl). They shift towards negative values at higher salt concentrations, resulting in larger discrepancies from experimental data. The FMAPP2



model exhibits a similar trend to xDLVO-CG calculations until around 0.2 M NaCl, but at higher ionic strengths, FMAPB2 fails to reproduce experimental trends of  $B_{22}$  of RbnA. The data indicate strong attractive interactions and fast decrease of  $B_{22}$ , which is not observed in experiment.  $B_{22}$  calculated with the xDLVO model fall outside the range of experimental values and the values calculated with xDLVO-CG and xDLVO-CGhybr. The positive shift throughout the entire salt concentration range is visible (see Fig. 4d), except at the highest ionic strength where it matches experimental data. This demonstrates once again that the proper representation of the protein shape is important for the  $B_{22}$  calculation. Since RbnA is far away from the spheric form (see Fig. 2b), standard DLVO methods cannot result in good agreements with experiments.

#### 4.3. Calculation of $B_{22}$ coefficients for medium-sized proteins

**Chymotrypsinogen A.** ChmT is a medium-sized protein with a globular shape, consisting of 245 residues (Fig. 6a). It serves as an inactive precursor of chymotrypsin, an enzyme that hydrolyzes peptide bonds between aromatic residues such as tyrosine, phenylalanine, and tryptophan.<sup>73</sup> In the present study, we calculated  $B_{22}$  values for ChmT at pH 3 and up to 1 M NaCl salt concentration (Fig. 6b). The values calculated by xDLVO-CGhybr values match nearly quantitatively with static light scattering measurements conducted by Velev *et al.*<sup>24</sup> and self-interaction chromatography measurements performed by Tessier *et al.*<sup>74</sup> Furthermore, a semi-quantitative agreement is observed with scattered light intensity measurements reported by Bajaj

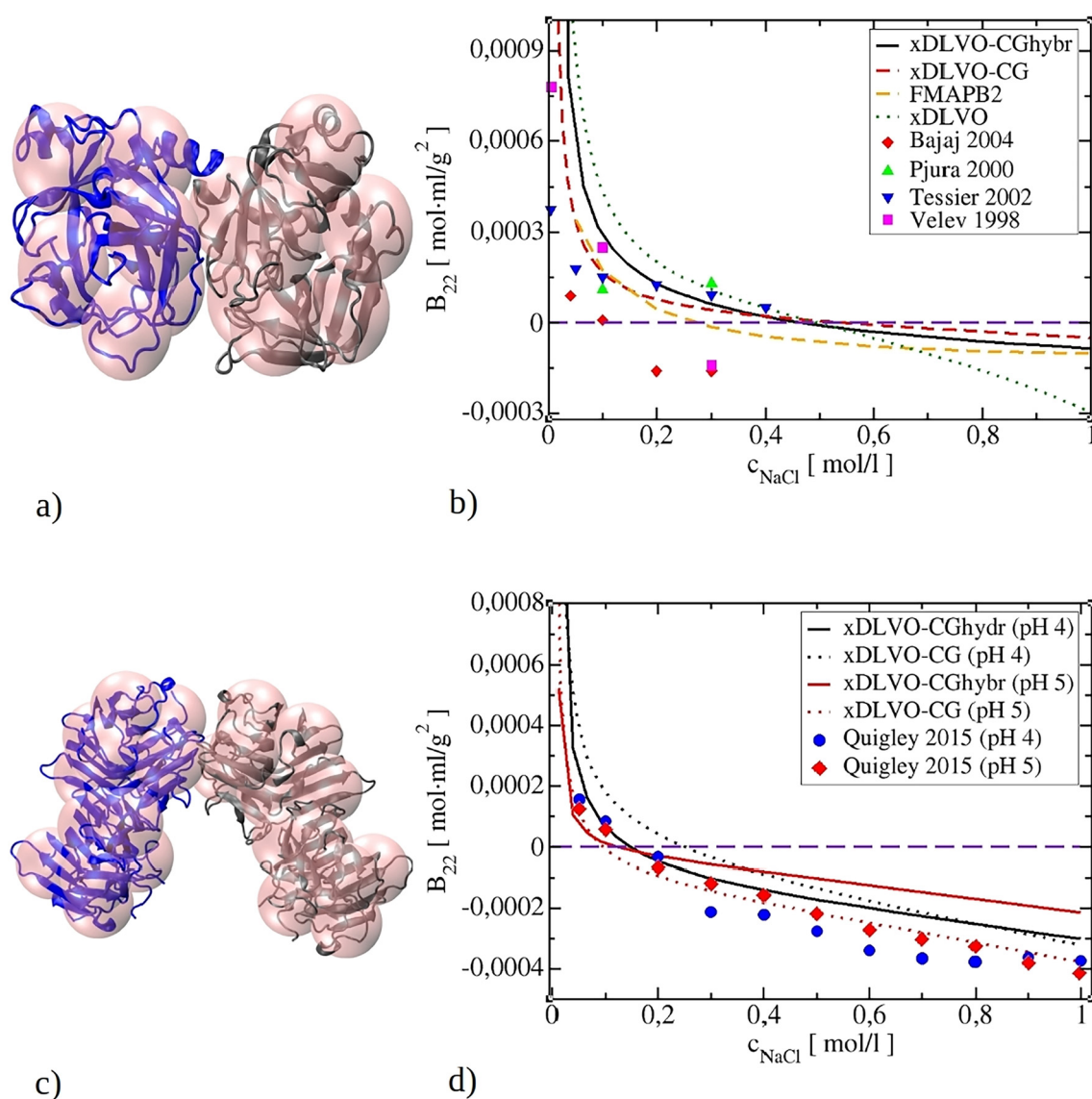


**Fig. 6** Visualisation of ChmT (a) and ConcA (c) proteins using the coarse-grained model implemented in xDLVO-CGhybr. The new cartoon representation of all-atom proteins is given for clarity. Calculated  $B_{22}$  coefficients by using xDLVO-CGhybr model and experimental results for ChmT at pH 3 (b). Data calculated by xDLVO-CG, FMAPB2 and xDLVO are marked by dashed red, dashed orange and green dots, respectively.  $B_{22}$  coefficients for ConcA at pH 4 and pH 5 (d) in comparison with reported experimental data.



*et al.*<sup>75</sup> and membrane osmometry measurements conducted by Pjura *et al.*<sup>76</sup> However, data calculated by the xDLVO-CG model are slightly negatively shifted compared to the data obtained by our new model. FMAPB2 calculations give data which are shifted towards negative values even more, especially at higher ionic strengths, indicating higher contribution of attractive PPIs. Values calculated by the xDLVO model are slightly positively shifted at low salt concentrations and towards negative at high salt concentrations. To the best of our knowledge, no experimental data were reported for concentrations higher than 0.4 M NaCl, making it difficult to compare the performance of these models at higher ionic strengths. Despite the variations in experimental  $B_{22}$  values, the  $B_{22}$  values calculated by xDLVO-CGhybr demonstrate a slightly more repulsive behaviour at lower ionic strengths. This trend aligns with the observations made in the Monte Carlo calculations of ChmT conducted by Lund *et al.*<sup>36</sup> and Neal *et al.*<sup>11</sup> In their studies, Lund *et al.* employed a residue-level coarse-grained model, while Neal *et al.* utilised an all-atom grained model to represent ChmT. Both studies reported similar behaviour regarding the repulsion at lower ionic strengths.

**Concanavalin A.** ConCA is a 50 kDa protein composed of 237 amino acid residues that exhibit a planar shape rich in antiparallel beta sheets (see Fig. 6c). Occurring naturally in jack-beans, ConCA is commonly used in biochemistry to characterise sugar-containing molecules and to purify glycosylated molecules in lectin-affinity chromatography.<sup>77</sup> The protein exhibits a specific dimer-tetramer equilibrium that depends on solution conditions.<sup>78,79</sup> It exists as a homodimer at pH lower than 7 and as a homotetramer at pH higher than 7.<sup>78–80</sup> In this study, we performed  $B_{22}$  calculations of ConCA at pH 4 and pH 5 and compared them with experimental values reported by Quigley *et al.*,<sup>7</sup> where self-interaction chromatography was used to measure  $B_{22}$  values.

Since ConCA predominantly exists as a dimer at the acidic pH range considered, calculations were performed between pairs of dimers (depicted in Fig. 6c). The experimental  $B_{22}$  measurements revealed that ConCA exhibits attractive PPIs, which cross the zero point at approximately 0.12 M NaCl.<sup>7</sup> The  $B_{22}$  coefficients calculated by the FMAPB2 and xDLVO models did not align with the experimental data and have therefore been omitted from the graph presented in Fig. 6d for simplicity (instead, see Fig. S3†). Our results show that both xDLVO-CGhybr and xDLVO-CG models can reproduce the general trends of experimental data and, more importantly, properly account repulsion interactions between dimers of ConCA in low ionic strengths, allowing to properly estimate its solubility and conditions, where aggregation happens. Overall, attractive interactions between proteins in solution are also well accounted for, however only till *ca.* 0.25 M NaCl. At higher salt concentrations, the agreement between theoretically and experimentally determined values is less quantitative than we have observed for other proteins.

At pH 4, the xDLVO-CG values are more positive than values reported in experiment, *i.e.* contribution of repulsion electrostatics is stronger than in other cases. The implementation of the new algorithm, where the electrostatic interactions are calculated on the smaller distances between proteins using PB, has significantly improved the quality of the  $B_{22}$  values, *i.e.* xDLVO-CGhybr model outperforms xDLVO-CG in this case. However, at pH 5, the xDLVO-CG model provides a nearly quantitative match with the experimentally measured data, therefore the performance of both methods shows the dependence on the pH used, which directly impacts the electrostatic potential on the protein surface. Nonetheless, since the xDLVO-CG model performs well only at one pH value, the strong agreement at pH 5 is more likely to be a coincidence than a systematic indication of its predictive capability. Therefore, we assume that limitations of the xDLVO-CGhybr model for the ConCA protein could be attributed to several factors. Firstly, the uncertainty in the correspondence between the protein charges assigned by the PROPKA method and the actual physical charges. Secondly, the ability of the protein to specifically absorb certain ions, which can alter its effective charge, is not accounted for in this model. Third, the ConCA protein and its dimer possess some degree of conformational flexibility<sup>80–82</sup> as a function of pH, which cannot be accounted for in our model which considers proteins like rigid bodies.

#### 4.4. $B_{22}$ calculations for large proteins

**Bovine serum albumin.** BSA is known for its remarkable ability to bind ligands such as drugs, nutrients, and metals.<sup>83</sup> With a mass of 65 kDa and an irregular shape (see Fig. 2e), BSA is composed of 583 amino acid residues. Its coarse-grained structure is modelled in the present study with 20 beads (see Fig. 7a). We performed calculations under conditions of pH 7.4 and NaCl concentration up to 1 M, and compared the results obtained with previously reported experimental values.<sup>23,26,84</sup>

As shown in Fig. 7b, calculations with xDLVO-CGhybr model yield significantly improved results compared to previous calculations using the xDLVO-CG model.<sup>54</sup> Calculated  $B_{22}$  values match the experimental values of Ma *et al.*<sup>26</sup> much better and keep the repulsive character of PPIs up to 1 M NaCl, following experimental trends. While at higher salt concentrations, the data calculated with xDLVO-CGhybr closely resembles the FMAPB2 data (based on all-atom structure of proteins), at lower ionic strengths, xDLVO-CGhybr exhibits significantly lower deviations from the experimentally measured values, indicating its better performance. In contrast, at NaCl salt concentration above 0.1 M, the spherical xDLVO model fails to properly reproduce  $B_{22}$  coefficients. The calculated values are decreasing abruptly towards the negative range, incorrectly predicting strong aggregation of BSA at these conditions. This highlights the limitations of simple spherical models like (x)DLVO in predicting the behaviour of complex proteins like BSA.





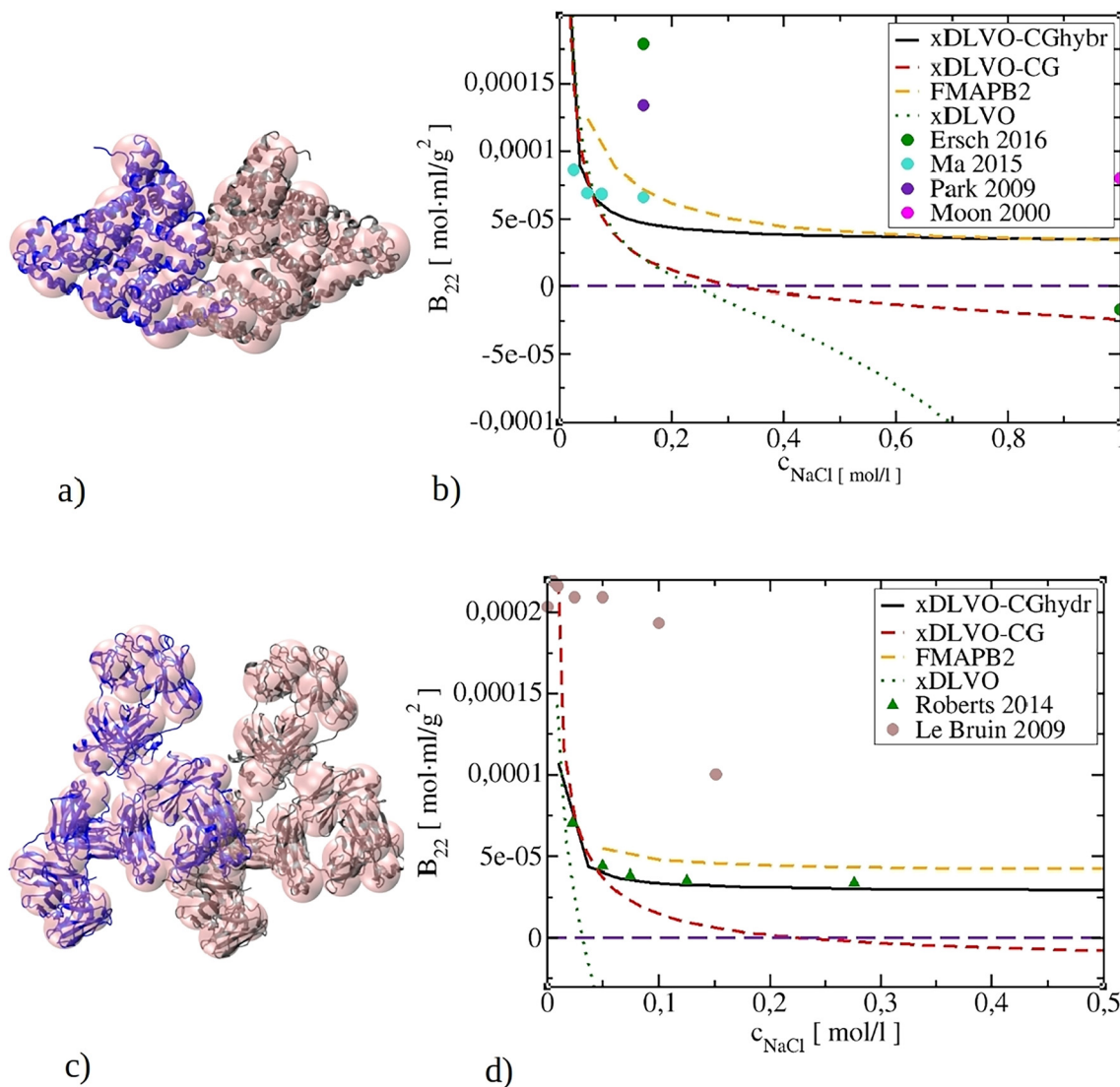


**Fig. 7** Visualisation of BSA (a) and IgG1 (c) proteins using the coarse-grained model implemented in xDLVO-CGhybr. The new cartoon representation of all-atom proteins is given for clarity. Calculated  $B_{22}$  coefficients for BSA at pH 7.4 (b) and IgG1 at pH 6.5 (d) as a function of NaCl concentration. Due to the computational cost of PB, twenty salt concentrations were used for the calculation of IgG1 in xDLVO-CGhybr.  $B_{22}$  values are compared with the values obtained with xDLVO-CG (dashed red), FMAPB2 (dashed orange) and xDLVO (green dots) models and experimental results (circles and triangles).

Therefore, such models rely heavily on fitted parameters to achieve quantitative agreement with experimental data. On the contrary, with hybrid treatment of the electrostatic interactions between proteins in the developed xDLVO-CGhybr model, the behaviour of BSA, in solutions under both low and high ionic strength conditions, are accurately predicted. This finding underscores the importance of developing more advanced models that incorporate the structural and dynamic complexities of proteins to better understand their behaviour in various environments.

**Human immunoglobulin type one.** IgG1 belongs to the subclass of monoclonal antibodies that play a critical role in the immune system's defence by recognizing and binding to specific antigens. These molecules have significant biotechnological and pharmaceutical importance, and many

are used in clinical therapies.<sup>85</sup> It is therefore crucial to develop formulations that remain stable in solution and do not undergo aggregation over time. IgG1 has a molecular mass of 13.9 kDa and a characteristic T-shaped structure (see Fig. 7c). It is composed of 644 residues and is modelled here with 40 CG beads. We performed calculations of IgG1 at pH 6.5 and compared them with experimental results reported in the literature.<sup>5,86</sup>

The  $B_{22}$  data calculated by xDLVO-CGhybr model, along with other models (refer to Fig. 7d), exhibit closer agreement with the experimental values reported by Roberts *et al.*<sup>86</sup> compared to the findings reported by Le Brun *et al.*<sup>5</sup> In the latter case, the higher  $B_{22}$  values indicate stronger repulsion interactions between proteins. In comparison to the xDLVO-CG model, yielding values that were closer to the



experimentally determined ones and similar to those obtained using the all-atom FMAPB2 model,<sup>54</sup> a clear improvement in the calculation of the second osmotic virial coefficients by the new model is visible (marked with the black line in Fig. 7d). In contrast, the simplified xDLVO model yielded data that are completely outside the experimental range, further highlighting its limited predictive power for large and irregular proteins.

IgG1 is the largest protein we have studied, and its complex shape highlights the need for more rigorous theoretical approaches to obtain more quantitative results. Still, we observe that improvement of the accuracy of the electrostatic interactions and the anisotropy of the protein shape refine the theoretical calculation of the  $B_{22}$  coefficients. Moreover, more experimental data points of  $B_{22}$  in diverse conditions would increase the validation set for future predictions. Several studies have been conducted using DLVO or xDLVO to model second osmotic coefficients of monoclonal antibodies in different solution conditions,<sup>27,33</sup> as well as to study its PPIs at higher protein concentrations.<sup>87</sup> These studies typically involved the use of various levels of coarse graining, and the models were often based on direct parametrization from experimental data.

#### 4.5. Modelling dispersion interactions: comparing Hamaker and Lennard-Jones potentials

The interaction between two molecules, as proposed by the Lifshitz theory of van der Waals forces, is rooted in the dipole field created by quantum fluctuations.<sup>44,88</sup> This results in mutual polarisation between molecules and with the solvent, giving rise to net attractive dispersion interactions.<sup>44,45,56</sup> The McLachlan formulation, which involves excess polarizability and dielectric permittivities at imaginary frequencies, can be used to calculate these interactions. However, modelling dispersion interactions is challenging, and the widely used Hamaker potential, which involves integrating the attractive part of Lennard-Jones potential between two homogeneous spheres, offers a simplified approach.<sup>57</sup> Nevertheless, determining the Hamaker constant according to Lifshitz–McLachlan theory is practically limited due to the requirement to know optical properties such as refractive indices and dielectric functions of proteins and solvent media.<sup>89</sup> As a result, other approaches are typically used in practice, such as fitting the Hamaker constant from experiments or using Lennard-Jones potential. Using Lennard-Jones parameters from all-atom force fields can result in interactions that are overly attractive, leading to overestimated assembly, *i.e.* negative  $B_{22}$  values. Empirical factors ranging from 0.1 to 0.3, which depend on the protein system being studied, are often used to scale these interactions.<sup>11,32,66,67</sup> Some researchers have attempted a hybrid approach, using LJ potential at short distances and Hamaker potential at larger distances, while scaling the LJ potential with an empirical factor to enable a smooth transition between potentials.<sup>67</sup>

In the present study, we have utilised LJ potentials to calculate dispersion interactions between proteins. They were scaled to match the depth of interaction of Hamaker potential with  $A_H$  obtained from literature (see Table S1†). To show the difference in the  $B_{22}$  calculation using LJ and Hamaker dispersion potentials, in Fig. 8 we demonstrate results for BPTI and IgG1 proteins using both approaches. We have observed that both LJ and Hamaker potential give similar  $B_{22}$  values, and correlate well with experimental data. While Hamaker potential is more convenient to use since it does not require additional parametrization, Lennard-Jones potential can better model anisotropy of dispersion interactions caused by protein orientations. Therefore, it may be preferable to use LJ potential in cases where more accurate and quantitative modelling is required.

It is important to note that current  $B_{22}$  models rely on the depth of dispersion interactions either through Hamaker constant or LJ scaling factor, thus, require further advancements in the field, particularly in simplifying the determination of dispersion interactions and Hamaker constants using Lifshitz–McLachlan theory for any protein system. These developments would greatly benefit predictive screening of solution conditions for desired protein phase behaviour. Finally, our results suggest that accurately evaluating electrostatic interactions is more crucial for improving the overall predictive power of the model, while the choice between Hamaker or Lennard-Jones potentials has less impact.

## Conclusions

In conclusion, we have developed the xDLVO-CGhybr model to accurately calculate the second osmotic virial coefficients of proteins at different pH as a function of the monovalent salt concentration. The new model represents a significant improvement over our previously reported xDLVO-CG model. By using a hybrid approach that combines Poisson–Boltzmann and Debye–Hückel theories, xDLVO-CGhybr more properly calculates the electrostatic contribution to the total interaction potential between proteins of arbitrary size and shape. Additionally, we have introduced a carefully parameterized coarse-grained Lennard-Jones potential in the PMF that enables accurate predictions of dispersion-based PPIs matched to the reference all-atom potentials.

To validate the accuracy of the model, we conducted extensive tests on six different proteins, ranging from small molecules like BPTI to large and complex proteins such as IgG1. Our results showed that the xDLVO-CGhybr model outperformed other theoretical models, such as xDLVO and FMAPB2, giving improved predictions of the  $B_{22}$  values. It enables the assessment of protein stability, solubility, and precise solubility calculations at different concentrations, pH values, and ionic strengths. These results demonstrate the potential of the xDLVO-CGhybr



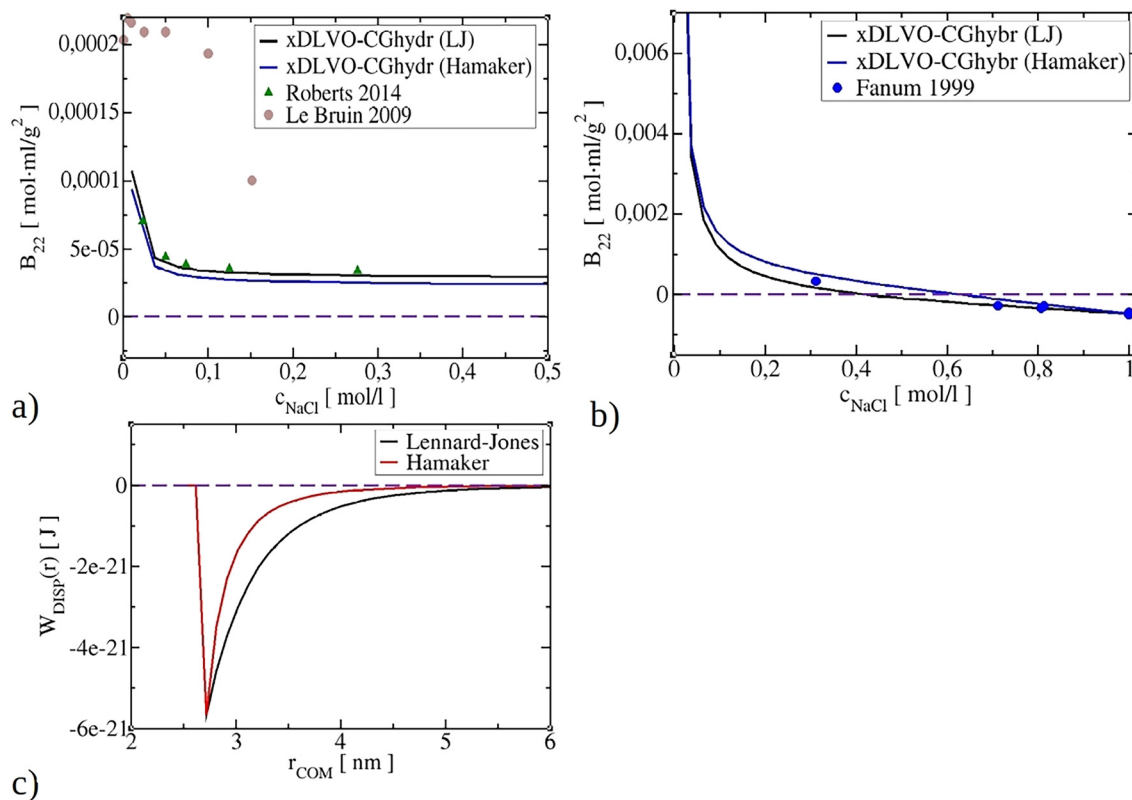


**Fig. 8** Impact of modelling dispersion interactions (Lennard-Jones or Hamaker dispersion) on the value of the  $B_{22}$  coefficients for IgG1 (a), BPTI (b). Comparison of Lennard-Jones versus Hamaker potential for BPTI (c).

model as a reliable tool for studying protein interactions and the behaviour of proteins in solution, particularly in the context of pharmaceutical and biotechnological applications. Moreover, the results obtained underscore the crucial role of accurate modelling of electrostatic interactions in determining overall PPIs in solution and the calculation of the  $B_{22}$  coefficients.

However, the xDLVO-CGhydr model does have certain limitations. It assumes rigid protein structures based on the available PDB database structures, while proteins in solution can undergo conformational changes that affect their interactions with other molecules. Additionally, the model's accuracy is influenced by the available protonation schemes, which may not fully capture the pH dependence of protein-protein interactions. Addressing these limitations and exploring alternative models that incorporate flexible structures and improved protonation schemes could enhance the accuracy and versatility of the model. Therefore, future developments may focus on advancing the xDLVO-CGhydr model by implementing advanced orientational sampling techniques that could efficiently explore relevant relative protein orientations, further improving predictions. Additionally, the integration of machine learning algorithms could enhance the speed and accuracy of the computation of interaction potential, expanding the model's scope and enabling more efficient exploration of parameter space.

## Author contributions

Conceptualization: S. P., W. W. and M. K.; methodology: S. P., W. W. and M. K.; software, S. P.; validation: S. P. and M. K.; formal analysis: S. P. and M. K.; investigation: S. P.; resources: W. W.; data curation: S. P.; writing – original draft preparation: S. P. and M. K.; writing – review and editing: S. P., W. W. and M. K.; visualisation: S. P.; supervision: W. W. and M. K.; project administration: M. K.; funding acquisition: W. W. All authors have read and agreed to the published version of the manuscript.

## Conflicts of interest

There are no conflicts to declare.

## Acknowledgements

This research has been funded by Deutsche Forschungsgemeinschaft (DFG) SPP priority programme DiSPBiotech (SPP1934, project number WE1863/30-2). W. W. and M. K. acknowledge funding by the DFG under the GRK 2450 “Scale bridging methods of computational nanoscience”.

## References

- 1 G. Chiesa, S. Kiriakov and A. S. Khalil, *BMC Biol.*, 2020, **18**, 35.
- 2 I. M. A. Nooren, *EMBO J.*, 2003, **22**, 3486–3492.



- 3 M. E. M. Cromwell, E. Hilario and F. Jacobson, *AAPS J.*, 2006, **8**, E572–E579.
- 4 A. C. A. Roque, C. R. Lowe and M. A. Taipa, *Biotechnol. Prog.*, 2004, **20**, 639–654.
- 5 V. Le Brun, W. Friess, S. Bassarab, S. Mühlau and P. Garidel, *Eur. J. Pharm. Biopharm.*, 2010, **75**, 16–25.
- 6 P. Braun and A.-C. Gingras, *Proteomics*, 2012, **12**, 1478–1498.
- 7 A. Quigley and D. R. Williams, *Eur. J. Pharm. Biopharm.*, 2015, **96**, 282–290.
- 8 S. D. Durbin and G. Feher, *Annu. Rev. Phys. Chem.*, 1996, **47**, 171–204.
- 9 R.-B. Zhou, H.-L. Cao, C.-Y. Zhang and D.-C. Yin, *CrystEngComm*, 2017, **19**, 1143–1155.
- 10 D. Leckband and S. Sivasankar, *Colloids Surf., B*, 1999, **14**, 83–97.
- 11 B. L. Neal, D. Asthagiri and A. M. Lenhoff, *Biophys. J.*, 1998, **75**, 2469–2477.
- 12 M. J. Uttinger, C. S. Hundschell, V. Lautenbach, S. Pusara, S. Bäther, T. R. Heyn, J. K. Keppler, W. Wenzel, J. Walter, M. Kozłowska, A. M. Wagemans and W. Peukert, *Soft Matter*, 2022, **18**, 6739–6756.
- 13 W. G. McMillan and J. E. Mayer, *J. Chem. Phys.*, 1945, **13**, 276–305.
- 14 L. F. M. Franco and P. de A. Pessôa Filho, *Braz. J. Chem. Eng.*, 2013, **30**, 95–104.
- 15 S. Ruppert, S. I. Sandler and A. M. Lenhoff, *Biotechnol. Prog.*, 2001, **17**, 182–187.
- 16 M. Herhut, C. Brandenbusch and G. Sadowski, *Fluid Phase Equilib.*, 2016, **422**, 32–42.
- 17 A. George, Y. Chiang, B. Guo, A. Arabshahi, Z. Cai and W. W. Wilson, in *Methods in Enzymology*, Elsevier, 1997, vol. 276, pp. 100–110.
- 18 B. Guo, S. Kao, H. McDonald, A. Asanov, L. L. Combs and W. W. Wilson, *J. Cryst. Growth*, 1999, **196**, 424–433.
- 19 A. C. Dumetz, A. M. Snellinger-O'Brien, E. W. Kaler and A. M. Lenhoff, *Protein Sci.*, 2007, **16**, 1867–1877.
- 20 M. Kastelic and V. Vlachy, *J. Phys. Chem. B*, 2018, **122**, 5400–5408.
- 21 J. Valente, R. Payne, M. Manning, W. Wilson and C. Henry, *Curr. Pharm. Biotechnol.*, 2005, **6**, 427–436.
- 22 A. George and W. W. Wilson, *Acta Crystallogr., Sect. D: Biol. Crystallogr.*, 1994, **50**, 361–365.
- 23 C. Ersch, L. L. C. Meijvogel, E. van der Linden, A. Martin and P. Venema, *Food Hydrocolloids*, 2016, **52**, 982–990.
- 24 O. D. Velev, E. W. Kaler and A. M. Lenhoff, *Biophys. J.*, 1998, **75**, 2682–2697.
- 25 F. Bonneté, S. Finet and A. Tardieu, *J. Cryst. Growth*, 1999, **196**, 403–414.
- 26 Y. Ma, D. M. Acosta, J. R. Whitney, R. Podgornik, N. F. Steinmetz, R. H. French and V. A. Parsegian, *J. Biol. Phys.*, 2015, **41**, 85–97.
- 27 D. Roberts, R. Keeling, M. Tracka, C. F. van der Walle, S. Uddin, J. Warwicker and R. Curtis, *Mol. Pharmaceutics*, 2014, **11**, 2475–2489.
- 28 B. L. Neal, D. Asthagiri, O. D. Velev, A. M. Lenhoff and E. W. Kaler, *J. Cryst. Growth*, 1999, **196**, 377–387.
- 29 D. J. Scott, T. R. Patel and D. J. Winzor, *Anal. Biochem.*, 2013, **435**, 159–165.
- 30 A. C. Stark, C. T. Andrews and A. H. Elcock, *J. Chem. Theory Comput.*, 2013, **9**, 4176–4185.
- 31 L. J. Quang, S. I. Sandler and A. M. Lenhoff, *J. Chem. Theory Comput.*, 2014, **10**, 835–845.
- 32 A. Grünberger, P.-K. Lai, M. A. Blanco and C. J. Roberts, *J. Phys. Chem. B*, 2013, **117**, 763–770.
- 33 C. Calero-Rubio, A. Saluja and C. J. Roberts, *J. Phys. Chem. B*, 2016, **120**, 6592–6605.
- 34 P. Mereghetti, R. R. Gabdouliline and R. C. Wade, *Biophys. J.*, 2010, **99**, 3782–3791.
- 35 S. R. McGuffee and A. H. Elcock, *J. Am. Chem. Soc.*, 2006, **128**, 12098–12110.
- 36 M. Lund and B. Jönsson, *Biophys. J.*, 2003, **85**, 2940–2947.
- 37 A. Jost Lopez, P. K. Quoika, M. Linke, G. Hummer and J. Köfinger, *J. Phys. Chem. B*, 2020, **124**, 4673–4685.
- 38 M. Boström, F. W. Tavares, B. W. Ninham and J. M. Prausnitz, *J. Phys. Chem. B*, 2006, **110**, 24757–24760.
- 39 M. Boström, F. W. Tavares, S. Finet, F. Skouri-Panet, A. Tardieu and B. W. Ninham, *Biophys. Chem.*, 2005, **117**, 217–224.
- 40 E. Hückel, in *Ergebnisse der exakten naturwissenschaften*, Springer Berlin Heidelberg, Berlin, Heidelberg, 1924, vol. 3, pp. 199–276.
- 41 D. E. Kuehner, H. W. Blanch and J. M. Prausnitz, *Fluid Phase Equilib.*, 1996, **116**, 140–147.
- 42 M. Herhut, C. Brandenbusch and G. Sadowski, *Biotechnol. J.*, 2016, **11**, 146–154.
- 43 M. Schleinitz, D. Teschner, G. Sadowski and C. Brandenbusch, *J. Mol. Liq.*, 2019, **283**, 575–583.
- 44 E. M. Lifshitz and M. Hamermesh, in *Perspectives in Theoretical Physics*, Elsevier, 1992, pp. 329–349.
- 45 J. Laven and J. P. C. Vissers, *Colloids Surf., A*, 1999, **152**, 345–355.
- 46 B. Kim and X. Song, *Phys. Rev. E*, 2011, **83**, 011915.
- 47 X. Song, *J. Chem. Phys.*, 2009, **131**, 044503.
- 48 N. A. Baker, D. Sept, S. Joseph, M. J. Holst and J. A. McCammon, *Proc. Natl. Acad. Sci. U. S. A.*, 2001, **98**, 10037–10041.
- 49 P. Ren, J. Chun, D. G. Thomas, M. J. Schnieders, M. Marucho, J. Zhang and N. A. Baker, *Q. Rev. Biophys.*, 2012, **45**, 427–491.
- 50 N. A. Baker, in *Methods in Enzymology*, Elsevier, 2004, vol. 383, pp. 94–118.
- 51 N. A. Baker, *Curr. Opin. Struct. Biol.*, 2005, **15**, 137–143.
- 52 M. Boström, F. W. Tavares, D. Bratko and B. W. Ninham, *J. Phys. Chem. B*, 2005, **109**, 24489–24494.
- 53 E. R. A. Lima, E. C. Biscaia, M. Boström, F. W. Tavares and J. M. Prausnitz, *J. Phys. Chem. C*, 2007, **111**, 16055–16059.
- 54 S. Pusara, P. Yamin, W. Wenzel, M. Krstić and M. Kozłowska, *Phys. Chem. Chem. Phys.*, 2021, **23**, 12780–12794.
- 55 S. Asakura and F. Oosawa, *J. Polym. Sci.*, 1958, **33**, 183–192.
- 56 S. Damodaran, *Biochemistry*, 2013, **52**, 8363–8373.
- 57 H. C. Hamaker, *Physica*, 1937, **4**, 1058–1072.





- 58 S. Damodaran, *Langmuir*, 2012, **28**, 9475–9486.
- 59 A. Arkhipov, P. L. Freddolino and K. Schulten, *Structure*, 2006, **14**, 1767–1777.
- 60 E. Jurrus, D. Engel, K. Star, K. Monson, J. Brandi, L. E. Felberg, D. H. Brookes, L. Wilson, J. Chen, K. Liles, M. Chun, P. Li, D. W. Gohara, T. Dolinsky, R. Konecny, D. R. Koes, J. E. Nielsen, T. Head-Gordon, W. Geng, R. Krasny, G. Wei, M. J. Holst, J. A. McCammon and N. A. Baker, *Protein Sci.*, 2018, **27**, 112–128.
- 61 T. J. Dolinsky, P. Czodrowski, H. Li, J. E. Nielsen, J. H. Jensen, G. Klebe and N. A. Baker, *Nucleic Acids Res.*, 2007, **35**, W522–W525.
- 62 J. Huang, S. Rauscher, G. Nawrocki, T. Ran, M. Feig, B. L. de Groot, H. Grubmüller and A. D. MacKerell, *Nat. Methods*, 2017, **14**, 71–73.
- 63 W. Humphrey, A. Dalke and K. Schulten, *J. Mol. Graphics*, 1996, **14**, 33–38.
- 64 S. T. Kottmann, *Theor. Chem. Acc.*, 2008, **119**, 421–427.
- 65 M. J. Abraham, T. Murtola, R. Schulz, S. Páll, J. C. Smith, B. Hess and E. Lindahl, *SoftwareX*, 2015, **1–2**, 19–25.
- 66 S. Qin and H.-X. Zhou, *J. Phys. Chem. B*, 2019, **123**, 8203–8215.
- 67 D. Asthagiri, B. L. Neal and A. M. Lenhoff, *Biophys. Chem.*, 1999, **78**, 219–231.
- 68 F. Pizzitutti, M. Marchi and D. Borgis, *J. Chem. Theory Comput.*, 2007, **3**, 1867–1876.
- 69 P. Ascenzi, A. Bocedi, M. Bolognesi, A. Spallarossa, M. Coletta, R. Cristofaro and E. Menegatti, *Curr. Protein Pept. Sci.*, 2003, **4**, 231–251.
- 70 M. Farnum and C. Zukoski, *Biophys. J.*, 1999, **76**, 2716–2726.
- 71 K. A. Dickson, M. C. Haigis and R. T. Raines, in *Progress in Nucleic Acid Research and Molecular Biology*, Elsevier, 2005, vol. 80, pp. 349–374.
- 72 P. M. Tessier, H. R. Johnson, R. Pazhianur, B. W. Berger, J. L. Prentice, B. J. Bahnson, S. I. Sandler and A. M. Lenhoff, *Proteins: Struct., Funct., Bioinf.*, 2002, **50**, 303–311.
- 73 K. A. Walsh and H. Neurath, *Proc. Natl. Acad. Sci. U. S. A.*, 1964, **52**, 884–889.
- 74 P. M. Tessier, A. M. Lenhoff and S. I. Sandler, *Biophys. J.*, 2002, **82**, 1620–1631.
- 75 H. Bajaj, V. K. Sharma and D. S. Kalonia, *Biophys. J.*, 2004, **87**, 4048–4055.
- 76 P. E. Pjura, A. M. Lenhoff, S. A. Leonard and A. G. Gittis, *J. Mol. Biol.*, 2000, **300**, 235–239.
- 77 H.-G. Schiefer, H. Krauss, H. Brunner and U. Gerhardt, *J. Bacteriol.*, 1975, **124**, 1598–1600.
- 78 D. F. Senear and D. C. Teller, *Biochemistry*, 1981, **20**, 3076–3083.
- 79 T. T. Herskovits, R. Jacobs and K. Nag, *Biochim. Biophys. Acta, Protein Struct. Mol. Enzymol.*, 1983, **742**, 142–154.
- 80 G. H. McKenzie, W. H. Sawyer and L. W. Nichol, *Biochim. Biophys. Acta, Protein Struct.*, 1972, **263**, 283–293.
- 81 H. E. Auer and T. Schilz, *Int. J. Pept. Protein Res.*, 2009, **24**, 462–471.
- 82 S. H. Koenig, R. D. Brown, C. F. Brewer and A. D. Sherry, *Biochem. Biophys. Res. Commun.*, 1982, **109**, 1047–1053.
- 83 T. Topalá, A. Bodoki, L. Oprean and R. Oprean, *Med. Pharm. Rep.*, 2014, **87**, 215–219.
- 84 Y. Park and G. Choi, *Korean J. Chem. Eng.*, 2009, **26**, 193–198.
- 85 M. S. Castelli, P. McGonigle and P. J. Hornby, *Pharmacol. Res. Perspect.*, 2019, **7**(6), e00535.
- 86 D. Roberts, R. Keeling, M. Tracka, C. F. van der Walle, S. Uddin, J. Warwicker and R. Curtis, *Mol. Pharmaceutics*, 2015, **12**, 179–193.
- 87 C. Calero-Rubio, R. Ghosh, A. Saluja and C. J. Roberts, *J. Pharm. Sci.*, 2018, **107**, 1269–1281.
- 88 C. M. Roth and A. M. Lenhoff, *J. Colloid Interface Sci.*, 1996, **179**, 637–639.
- 89 J.-L. Li, J. Chun, N. S. Wingreen, R. Car, I. A. Aksay and D. A. Saville, *Phys. Rev. B: Condens. Matter Mater. Phys.*, 2005, **71**, 235412.

